nanomaterials

MDPI

Article

Study on the Synthesis of Mn_3O_4 Nanooctahedrons and Their Performance for Lithium Ion Batteries

Yueyue Kong, Ranran Jiao, Suyuan Zeng *, Chuansheng Cui, Haibo Li, Shuling Xu and Lei Wang *

Department of Chemistry, Liaocheng University, Liaocheng, Shandong 252059, China; 15953766815@163.com (Y.K.); JRR1175@163.com (R.J.); cuichuansheng@lcu.edu.cn (C.C.); lihaibo@lcu.edu.cn (H.L.); xushuling@lcu.edu.cn (S.X.)

* Correspondence: drzengsy@163.com (S.Z.); wangl@ustc.edu (L.W.)

Received: 20 January 2020; Accepted: 18 February 2020; Published: 20 February 2020

Abstract: Among the transition metal oxides, the Mn_3O_4 nanostructure possesses high theoretical specific capacity and lower operating voltage. However, the low electrical conductivity of Mn_3O_4 decreases its specific capacity and restricts its application in the energy conversion and energy storage. In this work, well-shaped, octahedron-like Mn_3O_4 nanocrystals were prepared by one-step hydrothermal reduction method. Field emission scanning electron microscope, energy dispersive spectrometer, X-ray diffractometer, X-ray photoelectron spectrometer, high resolution transmission electron microscopy, and Fourier transformation infrared spectrometer were applied to characterize the morphology, the structure, and the composition of formed product. The growth mechanism of Mn_3O_4 nano-octahedron was studied. Cyclic voltammograms, galvanostatic charge–discharge, electrochemical impedance spectroscopy, and rate performance were used to study the electrochemical properties of obtained samples. The experimental results indicate that the component of initial reactants can influence the morphology and composition of the formed manganese oxide. At the current density of 1.0 A g^{-1}, the discharge specific capacity of as-prepared Mn_3O_4 nano-octahedrons maintains at about 450 mAh g^{-1} after 300 cycles. This work proves that the formed Mn_3O_4 nano-octahedrons possess an excellent reversibility and display promising electrochemical properties for the preparation of lithium-ion batteries.

Keywords: Mn_3O_4 nano-octahedrons; hydrothermal reduction method; structure characterization; electrochemical property; lithium-ion batteries

1. Introduction

In the past few years, lithium-ion batteries (LIBs) have increasingly held attention owing to their great potential in powering and in hybrid electric vehicles [1]. Thanks to their flexible structure and excellent chemical-physical properties, manganese-based materials (such as Mn_3O_4, MnO_2, and MnOOH) have been applied in the areas of energy storage and catalysis and attracted more interest [2,3]. Compared with other transition metal oxides, Mn_3O_4 nanostructure has higher theoretical specific capacity and lower operating voltage [4]; it has been considered as one of the promising electrode materials for the preparation of LIBs [5,6]. However, the low electrical conductivity and large volume change during charge/discharge processes decrease its specific capacity, render rapid capacity loss, and then restrict its applications in the energy conversion and energy storage [5,7].

Now, Mn_3O_4 materials with micro/nanosizes have been synthesized by a variety of methods, such as the hydrothermal method [8,9], solvothermal method [10], precipitation method [11], chemical decomposition [12], sputtering [13], electrodeposition [14], thermal decomposition [15], and so on. Mn_3O_4 nanoparticles with different morphologies have been successfully prepared. Generally, Mn_3O_4 materials were synthesized using commercial materials such as manganese sulphate [16], nitrate [17],

acetate [18–20], and $KMnO_4$ [21–24]. Han et al. produced Mn_3O_4 nano-particles using solvent evaporation technique from manganese acetyl acetonate [25]. Yue and Gu et al. synthesized hollow nano-spheres and hierarchical microspheres of MnO_2 materials using $KMnO_4$ and $MnSO_4$ via the hydrothermal method, and to obtain hollow nanospheres and hierarchical micro-spheres Mn_3O_4 [26,27]. Raj et al synthesized Mn_3O_4 by the reduction of $KMnO_4$ solution with hydrazine hydrate [21]. Thus, substantial efforts for the preparation of nanosized Mn_3O_4 have been performed to improve the electrochemical performance [3,28]. The LIBs prepared by Mn_3O_4 tetragonal bipyramids display high initial discharge capacity (1141.1 mAh g^{-1}), excellent reversible specific capacity (822.3 mAh g^{-1}), good rate performance, and higher coulombic efficiency [8]. Although much progress has been achieved, an effective, low-cost, and safe method to prepare Mn_3O_4 nano-octahedrons with uniform size to improve their electrochemical properties is highly desirable.

In this study, octahedron-like Mn_3O_4 nanostructures were prepared by the one-step hydrothermal reduction method. The nature of the formed manganese oxides can be effectively controlled by the initial reactant composition. A higher volume ratio of N-dimethylformamide (DMF) to $KMnO_4$ in the initial reaction solution contributes to the formation of pure Mn_3O_4 nano-octahedrons and the improvement of the capacity stability of the formed product.

2. Materials and Methods

2.1. Chemicals

Potassium permanganate ($KMnO_4$), N, N-dimethylformamide (DMF), anhydrous ethanol, acetylene black, polyvinylidene fluoride, N-methyl-pyrrolidone, metallic lithium, ethylene carbonate, and dimethyl carbonate were of analytical grade and purchased from Sinopharm Chemical Regent Co., Ltd. (Shanghai, China) The water used in the experiments was prepared from a Milli-Q water purification system (≥18 MΩ).

2.2. Synthesis of Mn_3O_4 Nano-Particles

In this work, Mn_3O_4 nano-particles could be prepared by a $KMnO_4$ hydrothermal reduction process. Firstly, 20 mL DMF was added into 20 mL 0.02 mol L^{-1} $KMnO_4$ aqueous solution under stirring, and the formed mixture was transformed into a Teflon-sealed autoclave. Then, the reaction system was heated to 150 °C and held for 9 h. Finally, the precipitates were collected by centrifugal separation, washed thoroughly with water and ethanol, and dried for testing. The obtained particles are Mn_3O_4 nano-octahedrons.

As 10 mL DMF was mixed with 30 mL 0.02 mol L^{-1} $KMnO_4$, and used as initial reactants for the above hydrothermal process, the obtained product contained MnOOH nano-columns and Mn_3O_4 nano-octahedrons and was named MnOOH/Mn_3O_4.

2.3. Material Characterization

The composition and phase of the obtained product were detected by an Ultima IV multipurpose X-ray diffraction system (XRD, Rigaku Corporation, Tokyo, Japan) using Cu Kα radiation (λ = 0.15406 nm). The morphology of formed sample was determined using a Sirion 200 field emission scanning electron microscope (FE-SEM, FEI Company, Eindhoven, Netherlands), while the chemical composition was characterized by an INCA energy dispersive spectrometer (EDS, Oxford Instruments, Oxon, England, UK). The lattice parameters and lattice images of as-prepared samples were tested by a Talos F200X field-emission high resolution transmission electron microscopy (FE-HRTEM, Thermo Fisher Scientific, Waltham, MA, USA). The surface constituents and element valence state of formed products were detected with an ESCLAB MKII X-ray photoelectron spectrometer (XPS, VG Scientific, Waltham, MA, USA). The binding energy of the obtained XPS spectra was calibrated by the C (1s) peak at 284.6 eV. The infrared absorption spectra were measured on a 6700 Fourier transformation infrared (FT-IR) spectrometer (Thermo Fisher Scientific, Waltham, MA, USA).

2.4. Electrochemical Measurements

In order to study the discharge/charge performances of Mn_3O_4 nano-octahedrons and MnOOH/Mn_3O_4, working electrodes were fabricated. The as-prepared manganese oxide, carbon black, and poly(vinylidene fluoride) were firstly blended in a weight ratio of 70:20:10. Then, N-methyl-pyrrolidone was added to prepare a paste. The formed slurry was homogeneously coated onto a copper foil, dried, and then used as anode. The assembly process of coin cells was conducted in a Mikrouna glove box. Metallic lithium and a polypropylene membrane with Celgard 2400 micropores were used as separator film and cathode, and 1 mol L^{-1} $LiPF_6$ was selected as the electrolyte.

Galvanostatic charge–discharge properties and rate capabilities of the formed LIBs were conducted on a CT2001A LAND battery test system. Cyclic voltammetry (CV) and electrochemical impedance spectroscopy (EIS) were determined by a Zennium-pro electrochemical workstation.

3. Results

3.1. Microstructure and Morphology

The microstructures of the obtained products were characterized by XRD, as shown in Figure 1. For the product prepared from 30 mL 0.02 mol L^{-1} $KMnO_4$ and 10 mL DMF, two phases that corresponded to MnOOH (JCPDS 74-1842) and Mn_3O_4 (JCPDS 24-0734) could be ascertained (Figure 1a). The diffraction peaks that correspond to the crystal planes of hausmannite Mn_3O_4 were labelled. The second phase represents an orthorhombic MnOOH, and the main diffraction peak at 26.30 degree corresponds to the crystal plane (110) of orthorhombic MnOOH. Other diffraction peaks at 34.15, 37.20, 39.80, 40.60, 55.10, and 71.70 degrees could be attributed to the (020), (101), (120), (200), (211), and (301) crystal planes of orthorhombic MnOOH, respectively.

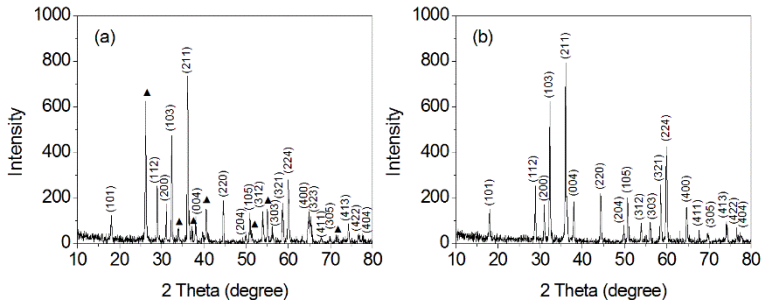

Figure 1. X-ray diffraction (XRD) patterns of obtained products prepared with different volume ratios of 0.02 mol L^{-1} $KMnO_4$ to N-dimethylformamide (DMF). (**a**) 3:1, (**b**) 1:1.

For the product prepared from 20 mL 0.02 mol L^{-1} $KMnO_4$ and 20 mL DMF, all the diffraction peaks can be indexed to the tetragonal hausmannite Mn_3O_4 (JCPDS 24-0734) (Figure 1b). The sharp peaks imply that the product possesses high crystalline quality. The results indicate that an increased volume ratio of DMF in the initial reactant solution contributes to the formation of pure Mn_3O_4 nanooctahedrons.

The morphology of the obtained sample was investigated by typical FE-SEM, as shown in Figure 2. For the mixture of MnOOH and Mn_3O_4, it contains two different nanostructures (Figure 2a–c). The long thin nano-columns are about 4.0 μm in length and 200 nm in diameter. Their aspect ratios are about 20. The nano-octahedrons are about 400 nm in an edge length. For the pure Mn_3O_4, nano octahedrons with uniform size, clear boundary, and point angle can be seen, and the mean edge length of nano-octahedron is about 400 nm (Figure 2d–f).

On the basis of the XRD patterns, we can assume that the formed nano-octahedrons correspond to Mn_3O_4, while the nano-columns can be attributed to the MOOH structure. FE-SEM images also demonstrate that the increased volume ratio of DMF in the initial reactant solution can contribute to the formation of pure Mn_3O_4 nano-octahedrons.

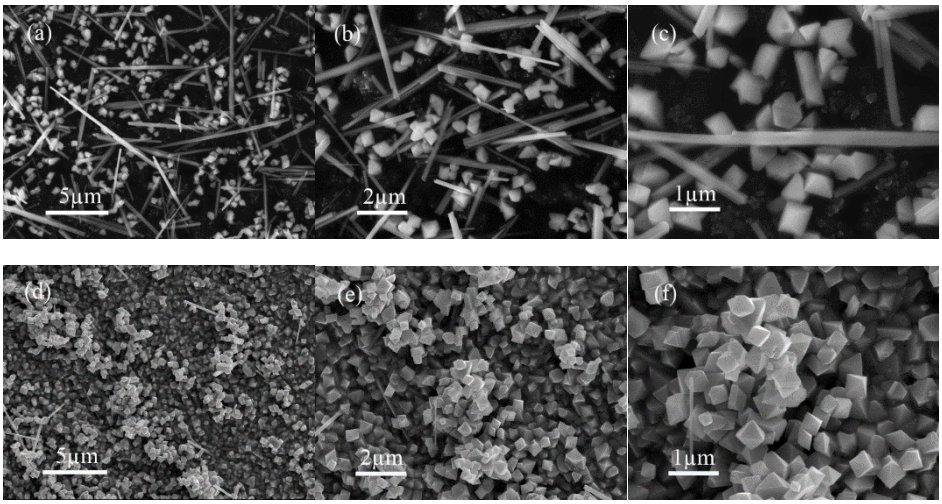

Figure 2. Field emission scanning electron microscope (FE-SEM) images of $MnOOH/Mn_3O_4$ (**a**–**c**) and pure Mn_3O_4 (**d**–**f**).

EDS was applied to determine the chemical composition of obtained samples, it confirms the existence of Mn and O. For the $MnOOH/Mn_3O_4$, the atomic ratio of Mn to O is 35.45:64.55 (Figure 3a), and the atomic ratio of Mn/O is less than 3:4, but larger than 1:2, which also suggests that the obtained product is the mixture of MnOOH and Mn_3O_4. For the Mn_3O_4 nano-octahedrons, the atomic ratio of Mn to O is 41.42:58.58, which is close to 3:4 and certifies the formation of Mn_3O_4.

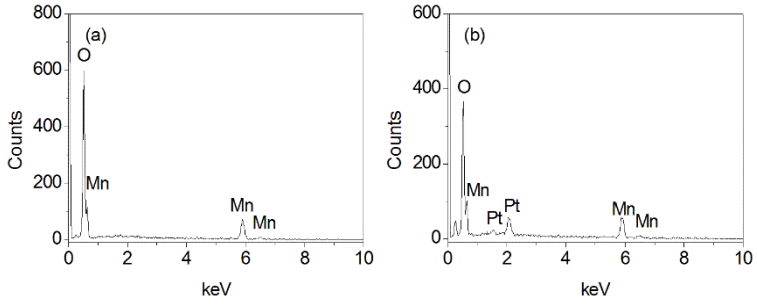

Figure 3. Energy dispersive spectrometer (EDS) of $MnOOH/Mn_3O_4$ (**a**) and Mn_3O_4 nanooctahedrons (**b**).

In the hydrothermal process, DMF plays an important role in chemical reaction and in oriented self-assembly. Firstly, DMF is one kind of Lewis base; it is easy to combine with H^+ in aqueous solution. So the initial reaction solution that contains DMF and $KMnO_4$ is alkaline. At the initial stage of the reaction, Mn^{3+} or MnOOH nuclei are formed as a sequence of the reduction of $KMnO_4$. Plenty of −OH groups in the water molecules would contribute to the formation of MnOOH and restrict the phase transformation of MnOOH to Mn_2O_3. At the same time, DMF was oxidized to *N*,*N*-dimethyl carbamic acid. The formation of N,N-dimethyl carbamic acid will change the pH value of the reaction solution, and act as a binding agent to control the nucleation and growth of crystals [29,30]. The formed nano-crystallites will accumulate and grow into lamellar MnOOH nano-structures. However, the formed lamellar nano-structures are just intermediates. As the reaction time is prolonged, lamellar MnOOH nano-structures will be re-dissolved and then grow into small nanowires as a result of the anisotropic growth [31,32]. The small nanowires prefer to combine with each other and grow into larger and longer nano-columns by the oriented attachment along their side surfaces [33]. As Mn^{2+} partially formed by further reduction of MnOOH, some octahedron-like Mn_3O_4 nanostructures began to occur. So the product obtained from the high volume ratio (3:1) of 0.02 mol L^{-1} $KMnO_4$ to DMF is the mixture of MnOOH nano-columns and Mn_3O_4 nano-octahedrons.

As the volume ratio of 0.02 mol L^{-1} $KMnO_4$ to DMF decreases to 1:1, the MnOOH nano-column will be reduced into Mn^{2+} by DMF. MnOOH nano-columns dissolve and disappear with the formation of octahedron-like nanostructures. It should be noted that DMF can coordinate with MnO^- and regulate the growth rate of Mn_3O_4 crystal by binding crystal facets [34,35]. The formed complex provides a suitable micro-environment for the formation of Mn_3O_4 nano-octahedrons [36,37]. At the same time, the pH value of the reaction system is important to the formation of uniform Mn_3O_4 nano-octahedrons. The increased volume ratio of DMF in the initial reactant solution means a higher pH value, which facilitates the growth along the <100> direction of Mn_3O_4. Furthermore, the ratio of crystal growth rate in the <100> direction to that in the <111> direction dominates the lattice structure and morphology of formed Mn_3O_4 [38]. Because the <111> plane of Mn_3O_4 has the lowest energy, eight stable crystal planes arrange on the surface of nano-octahedron. Finally, all of the products transformed into uniform nano-octahedrons with smooth surfaces. Under hydrothermal conditions, the coexistence of Mn^{2+} and Mn^{3+} facilitates the formation of the Mn_3O_4 crystal. So, the nature of formed manganese oxides can be effectively controlled by the initial reactant composition. Pure Mn_3O_4 nano-octahedrons can be synthesized by the higher volume ratio of DMF to $KMnO_4$ (1:1).

3.2. HR-TEM and Elemental Mapping

TEM can be used to observe the morphology of obtained manganese compounds. For the MnOOH/Mn_3O_4, nano-columns and nano-octahedrons can be identified, which is identical to FE-SEM images. The edge lengths of as-prepared nano-octahedrons are about 400 nm, while the formed nanocolumns are about 100–200 nm in diameter and up to 10 μm in length (Figure 4a,b). The interplanar distances calculated from the HR-TEM images are 0.219 and 0.262 nm (Figure 4c), which correspond to the (111) and (020) planes of monoclinic Mn_3O_4, respectively. The elemental mapping images demonstrated that Mn and O components are uniformly distributed all over the Mn_3O_4 nano-octahedrons and MnOOH nanocolumns (Figure 4d–f).

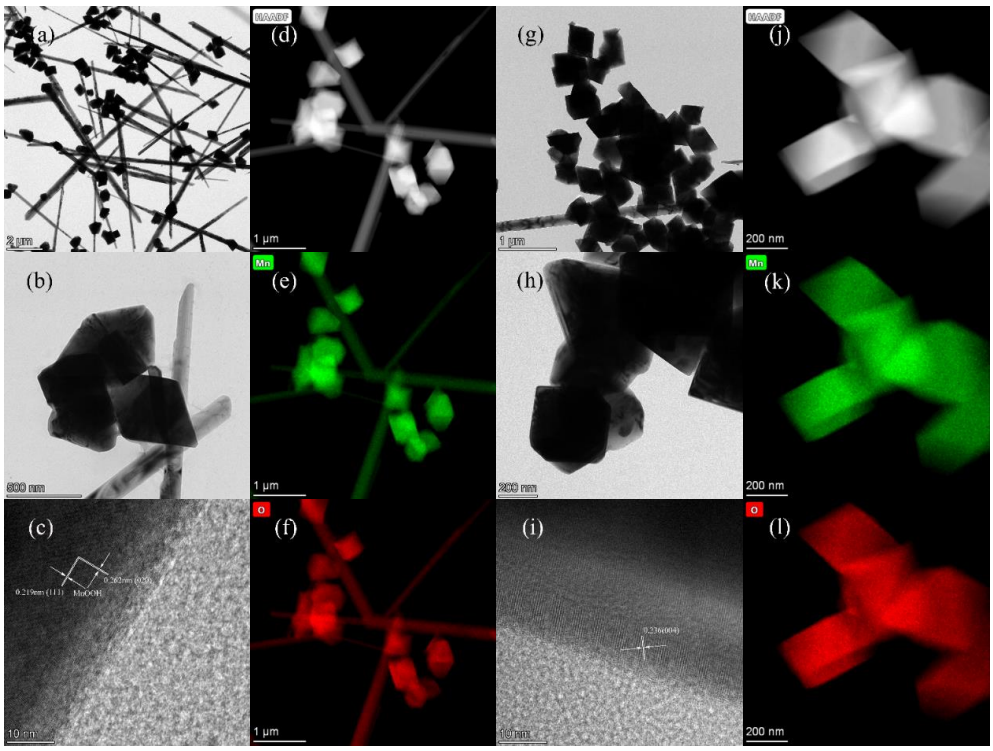

Figure 4. High resolution transmission electron microscopy (HR-TEM) and elemental mapping images of MnOOH/Mn_3O_4 (**a**–**f**) and Mn_3O_4 nanooctahedrons (**g**–**l**).

For the Mn_3O_4 nano-octahedrons, an average rhombic length of 300–500 nm can be found (Figure 4g–h), which is in agreement with the FE-SEM images. The HR-TEM image of an octahedral nanocrystal displays a lattice spacing of 0.236 nm (Figure 4i), and it can be assigned to the (004) plane of hausmannite Mn_3O_4 crystal [39]. Elemental dot-mapping images show that Mn and O components are evenly scattered throughout the nano-octahedrons (Figure 4j–l).

3.3. XPS Analysis

The surface composition and valence state of obtained products were analyzed by the XPS spectrum, as shown in Figure 5. For the MnOOH/Mn_3O_4, the Mn2p spectrum shows that the peaks of $Mn2p_{3/2}$ and $Mn2p_{1/2}$ center at 641.5 and 653.1 eV, respectively (Figure 5a). It can be deconvoluted into two pairs of doublets by fitting with the Gaussian function. The former doublet at 641.3 and 643.35 eV corresponds to Mn^{3+} $2p_{3/2}$ and Mn^{2+} $2p_{3/2}$, respectively, while the latter doublet at 652.90 and 654.45 eV could be attributed to Mn^{3+} $2p_{1/2}$ and Mn^{2+} $2p_{1/2}$, respectively [40]. Quantitative analysis indicates that the ratio of Mn^{2+}/Mn^{3+} is about 1:4. Considering the different valence ratio of the Mn element in the Mn_3O_4 and MnOOH, the above calculated value is reasonable. O 1s spectrum can be decomposed into three components (Figure 5b). The first peak at 529.65 eV is the characteristic of lattice oxygen, the second peak at 530.85 corresponds to the O^{2-} ions in oxygen vacancy defect regions, and the third peak at 531.55 eV is related to the adsorbed oxygen or dissociated oxygen [40,41]. The relative percentages of above three O components are 47.3%, 34.5%, and 18.2%.

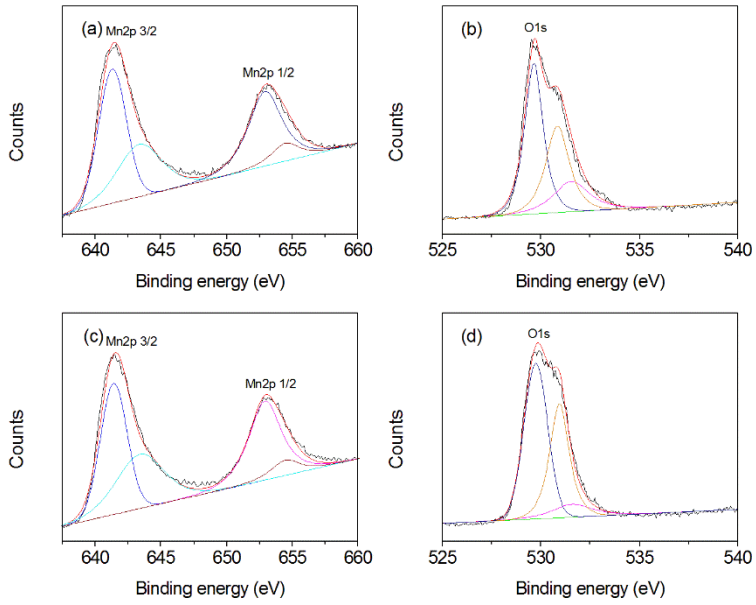

Figure 5. X-ray photoelectron spectrometer (XPS) spectra of MnOOH/Mn_3O_4 (**a**,**b**) and Mn_3O_4 nanooctahedrons (**c**,**d**).

For Mn_3O_4 nano-octahedrons, the Mn 2p XPS spectrum consisted of two spin-orbital lines (Figure 5c). The peaks at 641.50 and 653.20 eV are the characteristic peak of Mn $2p_{3/2}$ and Mn $2p_{1/2}$, respectively. A splitting of 11.7 eV occurs between Mn $2p_{1/2}$ and Mn $2p_{3/2}$, which is in agreement with the reported value of Mn_3O_4 [42,43]. Furthermore, the Mn 2p XPS spectrum could be divided into four components. The peaks at 641.4, 643.4, 652.90, and 654.45 eV can be ascribed to Mn^{3+} $2p_{3/2}$, Mn^{2+} $2p_{3/2}$, Mn^{3+} $2p_{1/2}$, and Mn^{2+} $2p_{1/2}$, respectively [40]. Quantitative analysis indicates that the ratio of Mn^{2+} to Mn^{3+} is about 0.5, which is consistent with the Mn components with different valence states in Mn_3O_4. O 1s spectrum of the formed nano-octahedrons can be resolved into three components with binding energies of 529.75, 530.95, and 532.4 eV (Figure 5d), which correspond to the lattice oxygen of Mn_3O_4, the O^{2-} ions of oxygen-vacancy defects within the matrix of Mn_3O_4 [41,44], and the adsorbed/dissociated

oxygen on the surface of Mn_3O_4 [40,41,45]. The relative percentages of above three O components are 55%, 36.7%, and 8.3%. The proportion of lattice oxygen in Mn_3O_4 nano-octahedrons is higher than that in the MnOOH/Mn_3O_4, while the proportion of adsorbed/dissociated oxygen species is lower. XPS analysis further confirms that the as-prepared nano-octahedrons are pure Mn_3O_4.

3.4. FT-IR Spectrum Analysis

FT-IR spectra can be used to confirm the formation of Mn_3O_4 and MnOOH [40,46]. For the MnOOH/Mn_3O_4 (Figure 6a), sharp peaks at 448, 491, and 593 cm^{-1} are the characteristic modes of Mn-O bonds in Mn_3O_4 and γ-MnOOH [47]. The peak at 418.6 and 531 cm^{-1} are the characteristic stretching mode and the bending mode of Mn-O bond at the octahedral sites of Mn_3O_4, respectively [48]. The peak at 632 cm^{-1} originated from the stretching vibrations of the Mn-O (Mn^{3+}) bond at the tetrahedral sites in the Mn_3O_4 [10,49]. The peak at 1085 cm^{-1} corresponds to the out-of-plane bending vibration of γ-OH, while the peaks at 1118 and 1151 cm^{-1} arise from the in-plane bending vibrations of δ-2-OH and δ-1-OH, respectively [50]. The above vibration absorption bands are consistent with that of the reported γ-MnOOH and hausmannite Mn_3O_4.

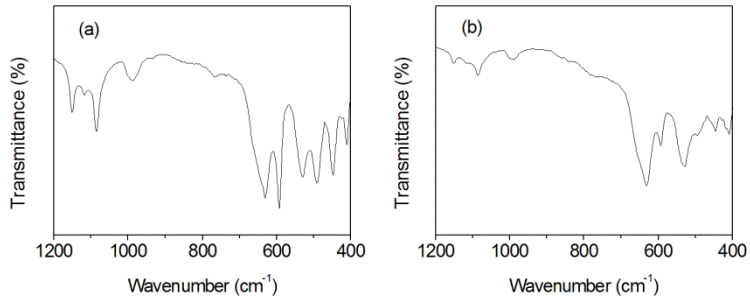

Figure 6. Fourier transformation infrared (FT-IR) of MnOOH /Mn_3O_4 (**a**) and Mn_3O_4 nanooctahedrons (**b**).

For the Mn_3O_4 nano-octahedrons (Figure 6b), the characteristic peak at 412 cm^{-1} is associated with the stretching mode of Mn-O-Mn bonds [51], the peak at 446 cm^{-1} comes from the band stretching modes of the octahedral sites [52]. The peak at 594 cm^{-1} is the characteristic band of Mn_3O_4, which corresponds to the stretching mode of the Mn-O bond at the tetrahedral site and the stretching mode of the Mn-O bond in an octahedral environment [53]. The peaks at 632 and 530 cm^{-1} originate from the coupling of Mn-O stretching vibrations at the tetrahedral site and at the octahedral site [54]. FT-IR measurement indicated that the obtained products are Mn_3O_4 nano-octahedrons.

3.5. Electrochemical Property

In this work, the galvanostatic charge–discharge process, CV, EIS, and rate capability were performed to compare the electrochemical properties of as-prepared samples.

During the galvanostatic measurements, the current density was set at 1.0 A g^{-1}, while the cutoff voltage was conducted within 0.01–3.0 V. The discharge/charge curves in initial three cycles were presented (Figure 7). For the MnOOH/Mn_3O_4 electrode, the discharge voltage drops steeply to 0.34 V. A long discharge voltage plateau at 0.3 V can be found in the first discharge curve, which comes from the reaction between MnOOH/Mn_3O_4 and Li [20,55]. In the second discharge process, the main voltage plateau at 0.58 V originates from the reaction between the MnO and Li, the formation of Mn and amorphous Li_2O [20]. In the third discharge curve, a discharge voltage plateau appears at 0.50 V. For the charging–discharging curves of the Mn_3O_4 nano-octahedrons electrode, a short voltage platform at 0.43 V can be found in the first discharging curves, which arises from the reaction occurred between Mn_3O_4 and metallic Li. In the second and third cycles, the discharge curves are coincided with each other, and the well-defined discharge voltage platform at 0.45 V originates from the reaction between the MnO and Li. The results indicate that the main discharge platform does not change obviously in the following cycles.

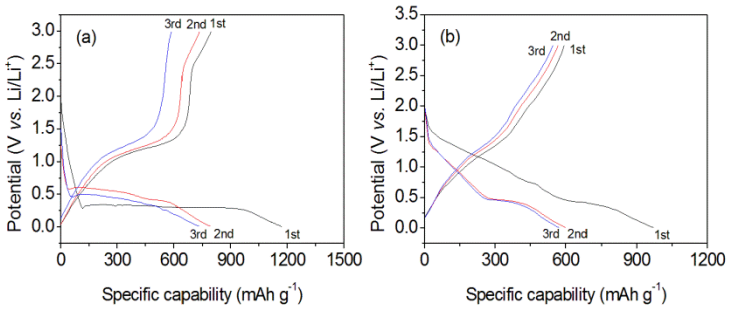

Figure 7. Galvanostatic charge/discharge profiles of MnOOH /Mn_3O_4 (**a**) and Mn_3O_4 nanooctahedrons (**b**) with a potential window from 0.01 V to 3.0 V at the current density of 1.0 A g^{-1}.

The long-term cyclabilities of as-prepared samples were recorded, as shown in Figure 8. For the MnOOH/Mn_3O_4 electrode, the specific capacities in the first discharge and charge processes are 1172.1 and 796.3 mAh g^{-1}. The low coulombic efficiency of 67.9% is related to the formation of solid electrolyte interphase (SEI) film [56]. However, the discharge and charge specific capacities decrease to 793.1 and 753.4 mAh g^{-1} in the second cycle. SEI films retard further lithiation of the inner part of Mn specimens and result in decreased discharge/charge capacity [57]. At the same time, the coulombic efficiency increases up to 92.7%. Cyclic performance examination reveals that the charge/discharge specific capacity continuously reduces to 391 mAh g^{-1} in the 73rd cycle. Since then, the discharge/charge specific capacity gradually increases. Finally, the discharge and charge capacity gradually increased to 724.2 and 722.4 mA h g^{-1} in the 300th cycle. Because the shape and size of formed MnOOH nano-columns and Mn_3O_4 nano-octahedrons are inhomogeneous, the cracking and fragmentation that originate from the stress during the lithiation reaction will lead to the increased discharge/charge specific capacity.

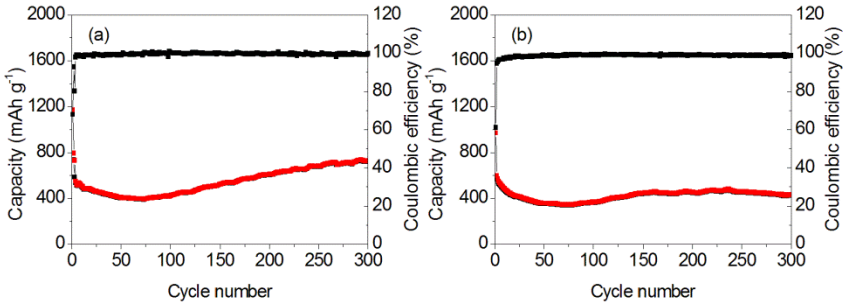

Figure 8. Cycle properties of MnOOH/Mn_3O_4 (**a**) and Mn_3O_4 nanooctahedrons (**b**) at the current density of 1.0 A g^{-1}.

For the Mn_3O_4 nano-octahedrons electrode, the discharge and charge specific capacities in the first cycle are 971.8 and 592.9 mAh g^{-1}, which reveals that the initial discharge capacity of octahedron-like Mn_3O_4 nano-structures measured at 1.0 A g^{-1} is higher than the theoretical capacity (937 mAh g^{-1}) for the conversion reaction to Mn and Li_2O [58]. In the second cycle, the discharge and charge specific capacity decreased to 599 and 567.4 mAh g^{-1}, while the coulombic efficiency increases up to 94.7%. In the 73rd cycle, the charge/discharge specific capacity reduces to 340 mAh g^{-1}. After that, it gradually increases. At the 150th cycle, the reversible specific capacity reaches 443 mAh g^{-1}. Since then, the charge/discharge specific capacity basically maintains at 450 mAh g^{-1}. Compared with the reported Mn_3O_4 nano-rods/wires [59], Mn_3O_4 nanotubes [60], Mn_3O_4 tetragonal bipyramids [8], Mn_3O_4 hierarchical microspheres [27,61], Mn_3O_4 hollow microspheres [62], Mn_3O_4 nanooctahedra [63], Mn_3O_4 nanosheets [64], and spherical-like Mn_3O_4-S nanoparticles [65], the formed Mn_3O_4 nano-octahedrons present better electrochemical properties.

Because the exposed (011) facets of as-prepared Mn_3O_4 nano-octahedrons are highly active, the improved cycling performance could be attributed to their smaller charge transfer resistance. At the same time, the alternating Mn and O atom layers on the exposed (011) facets can speed up the conversion reaction that occurs between Mn_3O_4 and Li, facilitate the multi-electron reaction, and ease the formation and decomposition of the amorphous Li_2O [63].

The details of the lithium insertion–extraction process can be evaluated by the CV method [66–68]. In this work, the initial three CV curves were recorded within 0.01–3.0 V at a scan rate of 0.1 mV s^{-1}, as shown in Figure 9.

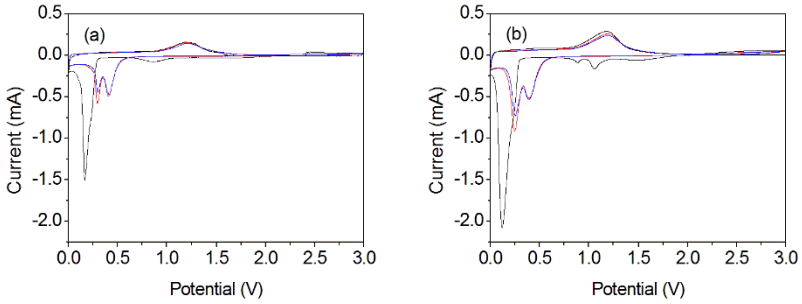

Figure 9. Cyclic voltammetry (CV) curves of MnOOH/Mn_3O_4 electrode (**a**) and Mn_3O_4 nanooctahedrons electrode (**b**).

For the MnOOH/Mn_3O_4 electrode, two reduction peaks can be found in the first cathodic sweep. The cathodic peaks centered at 0.166 and 0.86 V corresponded to the multistep lithium ion insertion mechanism, which included the reduction of Mn^{3+} to metallic Mn and the decomposition of organic electrolyte. The anodic peak that appeared at 1.21 V originated from the lithium ion extraction and oxidation of Mn to MnO [69]. In the following cycles, the cathodic peaks shifted to 0.30 and 0.41 V, demonstrating the occurrence of irreversible phase transformation after the first cycle. The first reduction peak may be mainly related to the drastic structural modifications that is impelled by lithium [70] and the reduction of MnO to metallic Mn [69], while the second reduction peak corresponds to the irreversible phase transformation during the lithium insertion in the first cycle [20,71,72]. In the initial three anodic sweeps, the oxidation peak is located at 1.2 V. Thus, equations of MnOOH nanocolumns/Mn_3O_4 nanooctahedrons electrode used for the rechargeable LIBs can be formulated [73]:

$$MnOOH + 3Li^+ + 3e^- \rightarrow Mn + Li_2O + LiOH \quad (1)$$

$$Mn_3O_4 + 8Li^+ + 8e^- \rightarrow 3Mn + 4Li_2O \quad (2)$$

$$Li_2O + Mn \rightarrow MnO + 2Li^+ + 2e^- \quad (3)$$

For the Mn_3O_4 nano-octahedrons electrode, three reduction peaks at 0.12, 0.88, and 1.06 V can be found in the first cathodic sweep. The intensive peak emerging at 0.12 V may be related to the reduction of Mn_3O_4 to MnO [71], the second peak locating at 0.88 V corresponds to the formation of the SEI layer on the electrode surface [69]. The third peak appearing at 1.06 V can be attributed to the reaction between Mn_3O_4 and Li during the process of the SEI layer formation [14]. The latter two weak peaks disappeared in the following cycles because they were annihilated in the next cycles [74]. The peak at 1.18 V in the first anodic sweep originated from the oxidation of Mn to MnO and reduction of Li_2O to Li [75]. In the second cycle, two reduction peaks are located at 0.25 V and 0.39 V, while the oxidation peak is much like that of the first anodic sweep. In the third cycle, the reduction/oxidation peaks are identical to those appeared in the second cycle, which indicate the good reversibility of Mn_3O_4 nano-octahedrons electrode [7,70,75]. So the electrochemical reaction that occurs in the first discharge/charge cycle will be summarized as the following equations [14,76,77]:

Initial discharge cycle

$$Mn_3O_4 + Li^+ + e^- \rightarrow LiMn_3O_4\left(1.5 - 0.5V vs Li^+/Li\right) \quad (4)$$

$$LiMn_3O_4 + Li^+ + e^- \rightarrow Li_2O + 3MnO\left(1.5 - 0.5V vs Li^+/Li\right) \quad (5)$$

$$MnO + 2Li^+ + 2e^- \rightarrow Mn + Li_2O\left(0.5 - 0.0V vs Li^+/Li\right) \quad (6)$$

Generally,

$$Mn_3O_4 + 8Li^+ + 8e^- \rightarrow 3Mn + 4Li_2O \quad (7)$$

Initial charge cycle:

$$Mn + Li_2O \rightarrow Mn + 2Li^+ + 2e^-\left(0.5 - 3.0V\ vs\ Li^+/Li\right) \quad (8)$$

Electrochemical impedance spectroscopy (EIS) was used to investigate the Mn_3O_4 electrodes. It can supply related information to compare the electrochemical, electron, and ion transport properties of different electrode materials [78–80]. The Nyquist plots as well as the equivalent electrical circuit for the prepared two Mn_3O_4 electrodes are shown in Figure 10a. The high frequency intercept on the real axis corresponds to the ohmic resistance (R_s), which originated from the electrolyte resistance, internal resistance of electrode, and contact resistance [81]. The results indicate that the R_s values of the MnOOH/Mn_3O_4 and pure Mn_3O_4 electrodes are 2.1 and 2.5 Ω, respectively. The semicircle in the high frequency region of Nyquist plot corresponds to charge-transfer resistance (R_{ct}). For the Mn_3O_4 nano-octahedrons electrode, the smaller diameter suggests that Mn_3O_4 nano-octahedrons possess a much lower charge transfer resistance (267.6 Ω) than that of the formed MnOOH/Mn_3O_4 (304.2 Ω). In addition, the slope of Nyquist plots in the low-frequency range of the EIS spectra correlates with the diffusion barrier of electrolyte ions. For Mn_3O_4 nano-octahedrons electrode, the much larger slope at low frequency intimated the faster electrolyte ion transfer than that in MnOOH/Mn_3O_4 electrodes (Figure 10b).

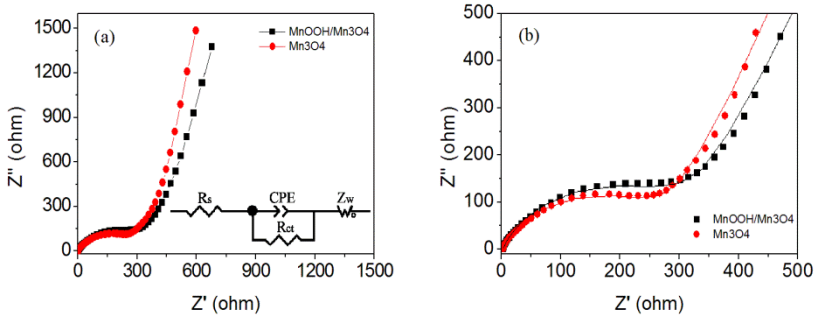

Figure 10. Nyquist plots of MnOOH/Mn_3O_4 and Mn_3O_4 electrodes (**a**) and the enlarged fitting plots (**b**). The inset shows the corresponding equivalent electrical circuit.

The rate capabilities were examined at the current densities of 0.2, 0.5, 1.0, 2.0, 5.0, and 0.20 A g^{-1}. The testing results were applied to compare the electrochemical characteristics of two formed samples, as shown in Figure 11. For the MnOOH /Mn_3O_4 electrode, the reversible specific capacities were 627, 516, 439, 368, 303, and 480 mAh g^{-1} (retention: 76.6%; 0.2–0.2 A g^{-1} in the last cycle) (Figure 11a). For the Mn_3O_4 nano-octahedrons electrode, the reversible specific capacity gradually decreases with the increase in the testing current density. The specific capacities of 1050, 840, 633, 475, 315, and 958 mAh g^{-1} are obtained. Even at a high current density of 5.0 A g^{-1}, Mn_3O_4 nano-octahedrons still deliver the specific capacity of 315 mAh g^{-1}. After the high current density of 5.0 A g^{-1} was conducted, the charge/discharge specific capacity measured at 0.2 A g^{-1} could be retrieved (retention: 91.2%; 0.2–0.2 A g^{-1} in the last cycle) (Figure 11b), which indicates that Mn_3O_4 nano-octahedrons

possess an excellent reversibility and display promising electrochemical properties as high capacity LIB electrode materials.

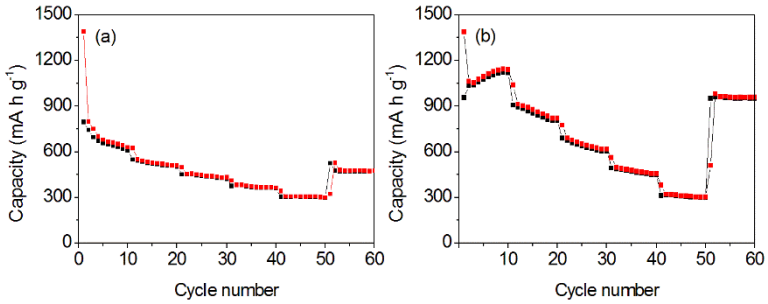

Figure 11. Rate performance of MnOOH/Mn_3O_4 electrode (**a**) and Mn_3O_4 nanooctahedrons electrode (**b**).

4. Conclusions

In this work, $KMnO_4$ and DMF were used for the preparation of Mn_3O_4 nano-octahedrons by the one-step hydrothemal reduction method. The structure, morphology, and composition of the obtained products were characterized, respectively. Galvanostatic charge–discharge, CV, EIS, and rate performance were used to study the electrochemical properties of obtained samples. The results indicated that the nature of as-prepared manganese oxides could be controlled by tuning the initial reactant composition. As the galvanostatic charge–discharge process was conducted at 1.0 A g^{-1}, the initial discharge-charge specific capacities of prepared Mn_3O_4 nano-octahedrons are 971.8 and 592.9 mAh g^{-1}. After 300 cycles, a discharge/charge specific capacity of 450 mAh g^{-1} can be delivered. The results indicated that the formed Mn_3O_4 nano-octahedrons possess outstanding capacity stability and can be used for the preparation of LIBs.

Author Contributions: Conceptualization, Y.K. and L.W.; Formal analysis, Y.K., R.J., S.Z., H.L. and S.X.; Investigation, K.Y., R.J., C.C. and S.X.; Software, R.J. and C.C.; Supervision, L.W.; Writing—original draft, Y.K. and R.J.; Writing—review, editing and submitting, S.Z. and L.W. All authors have read and agreed to the published version of the manuscript.

Funding: This work was financially supported by the Natural Science Foundation of Shandong Province (ZR2016BQ41, ZR2019MB064) and the Graduate Education Quality Promotion Program of Shandong Province (SDYY18186).

Conflicts of Interest: The authors declare no conflict of interest.

References

1. Luo, Y.; Fan, S.; Hao, N.; Zhong, S.; Liu, W. An ultrasound-assisted approach to synthesize Mn_3O_4/RGO hybrids with high capability for lithium ion batteries. *Dalton Trans.* **2014**, *43*, 15317–15320. [CrossRef] [PubMed]
2. Yan, W.; Kim, J.Y.; Xing, W.; Donavan, K.C.; Ayvazian, T.; Penner, R.M. Lithographically Patterned Gold/Manganese Dioxide Core/Shell Nanowires for High Capacity, High Rate, and High Cyclability Hybrid Electrical Energy Storage. *Chem. Mater.* **2012**, *24*, 2382–2390. [CrossRef]
3. Wang, D.; Li, Y.; Wang, Q.; Wang, T. Facile Synthesis of Porous Mn_3O_4 Nanocrystal–Graphene Nanocomposites for Electrochemical Supercapacitors. *Eur. J. Inorg. Chem.* **2012**, *2012*, 628–635. [CrossRef]
4. Bai, Z.; Fan, N.; Sun, C.; Ju, Z.; Guo, C.; Yang, J.; Qian, Y. Facile synthesis of loaf-like ZnMn2O4 nanorods and their excellent performance in Li-ion batteries. *Nanoscale* **2013**, *5*, 2442–2447. [CrossRef] [PubMed]
5. Wang, H.; Cui, L.-F.; Yang, Y.; Sanchez Casalongue, H.; Robinson, J.T.; Liang, Y.; Cui, Y.; Dai, H. Mn_3O_4-Graphene Hybrid as a High-Capacity Anode Material for Lithium Ion Batteries. *J. Am. Chem. Soc.* **2010**, *132*, 13978–13980. [CrossRef]
6. Lee, J.W.; Hall, A.S.; Kim, J.-D.; Mallouk, T.E. A Facile and Template-Free Hydrothermal Synthesis of Mn_3O_4 Nanorods on Graphene Sheets for Supercapacitor Electrodes with Long Cycle Stability. *Chem. Mater.* **2012**, *24*, 1158–1164. [CrossRef]

7. Wang, C.; Yin, L.; Xiang, D.; Qi, Y. Uniform Carbon Layer Coated Mn_3O_4 Nanorod Anodes with Improved Reversible Capacity and Cyclic Stability for Lithium Ion Batteries. *ACS Appl. Mater. Interfaces* **2012**, *4*, 1636–1642. [CrossRef]
8. Li, T.; Guo, C.; Sun, B.; Li, T.; Li, Y.; Hou, L.; Wei, Y. Well-shaped Mn_3O_4 tetragonal bipyramids with good performance for lithium ion batteries. *J. Mater. Chem. A* **2015**, *3*, 7248–7254. [CrossRef]
9. Shaik, D.P.M.D.; Rosaiah, P.; Hussain, O.M. Supercapacitive Performance of Mn_3O_4 Nanoparticles Synthesized by Hydrothermal Method. *Adv. Sci. Eng. Med.* **2016**, *8*, 140–145. [CrossRef]
10. Duan, J.; Zheng, Y.; Chen, S.; Tang, Y.; Jaroniec, M.; Qiao, S. Mesoporous hybrid material composed of Mn_3O_4 nanoparticles on nitrogen-doped graphene for highly efficient oxygen reduction reaction. *Chem. Commun.* **2013**, *49*, 7705–7707. [CrossRef]
11. Gao, J.; Lowe, M.A.; Abruña, H.D. Spongelike Nanosized Mn_3O_4 as a High-Capacity Anode Material for Rechargeable Lithium Batteries. *Chem. Mater.* **2011**, *23*, 3223–3227. [CrossRef]
12. Subramani, K.; Jeyakumar, D.; Sathish, M. Manganese hexacyanoferrate derived Mn_3O_4 nanocubes-reduced graphene oxide nanocomposites and their charge storage characteristics in supercapacitors. *Phys. Chem. Chem. Phys.* **2014**, *16*, 4952–4961. [CrossRef] [PubMed]
13. Gorlin, Y.; Chung, C.-J.; Nordlund, D.; Clemens, B.M.; Jaramillo, T.F. Mn_3O_4 Supported on Glassy Carbon: An Active Non-Precious Metal Catalyst for the Oxygen Reduction Reaction. *ACS Catal.* **2012**, *2*, 2687–2694. [CrossRef]
14. Fan, X.-Y.; Cui, Y.; Liu, P.; Gou, L.; Xu, L.; Li, D.-L. Electrochemical construction of three-dimensional porous Mn_3O_4 nanosheet arrays as an anode for the lithium ion battery. *Phys. Chem. Chem. Phys.* **2016**, *18*, 22224–22234. [CrossRef] [PubMed]
15. Jiangying, Q.; Feng, G.; Quan, Z.; Zhiyu, W.; Han, H.; Beibei, L.; Wubo, W.; Xuzhen, W.; Jieshan, Q. Highly atom-economic synthesis of graphene/Mn_3O_4 hybrid composites for electrochemical supercapacitors. *Nanoscale* **2013**, *5*, 2999–3005. [CrossRef] [PubMed]
16. Li, X.; Song, H.; Wang, H.; Zhang, Y.; Du, K.; Li, H.; Huang, J. A nanocomposite of graphene/MnO_2 nanoplatelets for high-capacity lithium storage. *J. Appl. Electrochem.* **2012**, *42*, 1065–1070. [CrossRef]
17. Chae, C.; Kim, J.H.; Kim, J.M.; Sun, Y.-K.; Lee, J.K. Highly reversible conversion-capacity of MnOx-loaded ordered mesoporous carbon nanorods for lithium-ion battery anodes. *J. Mater. Chem.* **2012**, *22*, 17870–17877. [CrossRef]
18. Rosaiah, P.; Zhu, J.; Shaik PMD, D.; Hussain, O.M.; Qiu, Y.; Zhao, L. Reduced graphene oxide/Mn_3O_4 nanocomposite electrodes with enhanced electrochemical performance for energy storage applications. *J. Electroanal. Chem.* **2017**, *794*, 78–85. [CrossRef]
19. Wang, J.-G.; Jin, D.; Zhou, R.; Li, X.; Liu, X.-r.; Shen, C.; Xie, K.; Li, B.; Kang, F.; Wei, B. Highly Flexible Graphene/Mn_3O_4 Nanocomposite Membrane as Advanced Anodes for Li-Ion Batteries. *ACS Nano* **2016**, *10*, 6227–6234. [CrossRef]
20. Li, L.; Guo, Z.; Du, A.; Liu, H. Rapid microwave-assisted synthesis of Mn_3O_4-graphene nanocomposite and its lithium storage properties. *J. Mater. Chem.* **2012**, *22*, 3600–3605. [CrossRef]
21. Bag, S.; Roy, K.; Gopinath, C.S.; Raj, C.R. Facile Single-Step Synthesis of Nitrogen-Doped Reduced Graphene Oxide-Mn_3O_4 Hybrid Functional Material for the Electrocatalytic Reduction of Oxygen. *ACS Appl. Mater. Interfaces* **2014**, *6*, 2692–2699. [CrossRef] [PubMed]
22. Li, J.; Zou, M.; Zhao, Y.; Lin, Y.; Lai, H.; Guan, L.; Huang, Z. Coaxial MWNTs@MnO_2 confined in conducting PPy for kinetically efficient and long-term lithium ion storage. *Electrochim. Acta* **2013**, *111*, 165–171. [CrossRef]
23. Li, Y.; Ye, D.; Liu, W.; Shi, B.; Guo, R.; Zhao, H.; Pei, H.; Xu, J.; Xie, J. A MnO_2/Graphene Oxide/Multi-Walled Carbon Nanotubes-Sulfur Composite with Dual-Efficient Polysulfide Adsorption for Improving Lithium-Sulfur Batteries. *ACS Appl. Mater. Interfaces* **2016**, *8*, 28566–28573. [CrossRef] [PubMed]
24. Xia, H.; Lai, M.; Lu, L. Nanoflaky MnO_2/carbon nanotube nanocomposites as anode materials for lithium-ion batteries. *J. Mater. Chem.* **2010**, *20*, 6896–6902. [CrossRef]
25. Han, Y.-F.; Chen, F.; Zhong, Z.; Ramesh, K.; Chen, L.; Widjaja, E. Controlled Synthesis, Characterization, and Catalytic Properties of Mn_2O_3 and Mn_3O_4 Nanoparticles Supported on Mesoporous Silica SBA-15. *J. Phys. Chem. B* **2006**, *110*, 24450–24456. [CrossRef] [PubMed]

26. Yue, J.; Gu, X.; Chen, L.; Wang, N.; Jiang, X.; Xu, H.; Yang, J.; Qian, Y. General synthesis of hollow MnO_2, Mn_3O_4 and MnO nanospheres as superior anode materials for lithium ion batteries. *J. Mater. Chem. A* **2014**, *2*, 17421–17426. [CrossRef]
27. Gu, X.; Yue, J.; Li, L.; Xue, H.; Yang, J.; Zhao, X. General Synthesis of MnOx (MnO_2, Mn_2O_3, Mn_3O_4, MnO) Hierarchical Microspheres as Lithium-ion Battery Anodes. *Electrochim. Acta* **2015**, *184*, 250–256. [CrossRef]
28. Hu, C.-C.; Wu, Y.-T.; Chang, K.-H. Low-Temperature Hydrothermal Synthesis of Mn_3O_4 and MnOOH Single Crystals: Determinant Influence of Oxidants. *Chem. Mater.* **2008**, *20*, 2890–2894. [CrossRef]
29. Golmojdeh, H.; Zanjanchi, M.A. A facile approach for synthesis of $BiVO_4$ nano-particles possessing high surface area and various morphologies. *Cryst. Res. Technol.* **2012**, *47*, 1014–1025. [CrossRef]
30. Zhou, X.; Fu, W.; Yang, H.; Ma, D.; Cao, J.; Leng, Y.; Guo, J.; Zhang, Y.; Sui, Y.; Zhao, W.; et al. Synthesis and ethanol-sensing properties of flowerlike SnO2 nanorods bundles by poly(ethylene glycol)-assisted hydrothermal process. *Mater. Chem. Phys.* **2010**, *124*, 614–618. [CrossRef]
31. Wang, X.; Li, Y. Synthesis and Formation Mechanism of Manganese Dioxide Nanowires/Nanorods. *Chem. Eur. J.* **2003**, *9*, 300–306. [CrossRef] [PubMed]
32. Yang, J.; Zeng, J.-H.; Yu, S.-H.; Yang, L.; Zhou, G.-e.; Qian, Y.-t. Formation Process of CdS Nanorods via Solvothermal Route. *Chem. Mater.* **2000**, *12*, 3259–3263. [CrossRef]
33. Lan, L.; Li, Q.; Gu, G.; Zhang, H.; Liu, B. Hydrothermal synthesis of γ-MnOOH nanorods and their conversion to MnO_2, Mn_2O_3, and Mn_3O_4 nanorods. *J. Alloys Compd.* **2015**, *644*, 430–437. [CrossRef]
34. Rajput, L.; Biradha, K. Bimetallic Clusters of Pyridine-Appended Ethylenediaminetetraacetic Acid (EDTA)-amides in Designing 1D and 2D Coordination Frameworks. *Cryst. Growth Des.* **2007**, *7*, 2376–2379. [CrossRef]
35. Jiang, H.; Hu, J.; Li, C.; Gu, F.; Ma, J. Large-scale, uniform, single-crystalline Cd(OH)2 hexagonal platelets for Cd-based functional applications. *CrystEngComm* **2010**, *12*, 1726–1729. [CrossRef]
36. Jiang, H.; Zhao, T.; Yan, C.; Ma, J.; Li, C. Hydrothermal synthesis of novel Mn_3O_4 nano-octahedrons with enhanced supercapacitors performances. *Nanoscale* **2010**, *2*, 2195–2198. [CrossRef]
37. Zhang, D.; Zhang, X.; Ni, X.; Song, J.; Zheng, H. Fabrication and Characterization of Fe3O4 Octahedrons via an EDTA-Assisted Route. *Cryst. Growth Des.* **2007**, *7*, 2117–2119. [CrossRef]
38. Wang, Z.L. Transmission Electron Microscopy of Shape-Controlled Nanocrystals and Their Assemblies. *J. Phys. Chem. B* **2000**, *104*, 1153–1175. [CrossRef]
39. Yin, J.; Gao, F.; Wu, Y.; Wang, J.; Lu, Q. Synthesis of Mn_3O_4 octahedrons and other manganese-based nanostructures through a simple and green route. *CrystEngComm* **2010**, *12*, 3401–3403. [CrossRef]
40. Tian, Z.-Y.; Mountapmbeme Kouotou, P.; Bahlawane, N.; Tchoua Ngamou, P.H. Synthesis of the Catalytically Active Mn_3O_4 Spinel and Its Thermal Properties. *J. Phys. Chem. C* **2013**, *117*, 6218–6224. [CrossRef]
41. Han, X.G.; He, H.Z.; Kuang, Q.; Zhou, X.; Zhang, X.H.; Xu, T.; Xie, Z.X.; Zheng, L.S. Controlling Morphologies and Tuning the Related Properties of Nano/Microstructured ZnO Crystallites. *J. Phys. Chem. C* **2009**, *113*, 584–589. [CrossRef]
42. Tian, Z.-Y.; Tchoua Ngamou, P.H.; Vannier, V.; Kohse-Höinghaus, K.; Bahlawane, N. Catalytic oxidation of VOCs over mixed Co–Mn oxides. *Appl. Catal. B Environ* **2012**, *117–118*, 125–134. [CrossRef]
43. Todorova, S.; Kolev, H.; Holgado, J.P.; Kadinov, G.; Bonev, C.; Pereñíguez, R.; Caballero, A. Complete n-hexane oxidation over supported Mnn-Co catalysts. *Appl. Catal. B Environ.* **2010**, *94*, 46–54. [CrossRef]
44. Zhang, Y.; Du, G.; Wang, X.; Li, W.; Yang, X.; Ma, Y.; Zhao, B.; Yang, H.; Liu, D.; Yang, S. X-ray photoelectron spectroscopy study of ZnO films grown by metal-organic chemical vapor deposition. *J. Cryst. Growth* **2003**, *252*, 180–183. [CrossRef]
45. Wang, Z.G.; Zu, X.T.; Zhu, S.; Wang, L.M. Green luminescence originates from surface defects in ZnO nanoparticles. *Phys. E* **2006**, *35*, 199–202. [CrossRef]
46. Wang, Y.; Zhu, L.; Yang, X.; Shao, E.; Deng, X.; Liu, N.; Wu, M. Facile synthesis of three-dimensional Mn_3O_4 hierarchical microstructures and their application in the degradation of methylene blue. *J. Mater. Chem. A* **2015**, *3*, 2934–2941. [CrossRef]
47. Li, Z.; Bao, H.; Miao, X.; Chen, X. A facile route to growth of γ-MnOOH nanorods and electrochemical capacitance properties. *J. Colloid Interf. Sci.* **2011**, *357*, 286–291. [CrossRef]
48. Zhang, W.; Yang, Z.; Liu, Y.; Tang, S.; Han, X.; Chen, M. Controlled synthesis of Mn_3O_4 nanocrystallites and MnOOH nanorods by a solvothermal method. *J. Cryst. Growth* **2004**, *263*, 394–399. [CrossRef]

49. Li, Y.; Li, X.-M. Facile treatment of wastewater produced in Hummer's method to prepare Mn_3O_4 nanoparticles and study their electrochemical performance in an asymmetric supercapacitor. *RSC Adv.* **2013**, *3*, 2398–2403. [CrossRef]
50. Sharma, P.K.; Whittingham, M.S. The role of tetraethyl ammonium hydroxide on the phase determination and electrical properties of γ-MnOOH synthesized by hydrothermal. *Mater. Lett.* **2001**, *48*, 319–323. [CrossRef]
51. Giri, A.; Goswami, N.; Pal, M.; Zar Myint, M.T.; Al-Harthi, S.; Singha, A.; Ghosh, B.; Dutta, J.; Pal, S.K. Rational surface modification of Mn_3O_4 nanoparticles to induce multiple photoluminescence and room temperature ferromagnetism. *J. Mater. Chem. C* **2013**, *1*, 1885–1895. [CrossRef]
52. Wang, M.; Cheng, L.; Li, Q.; Chen, Z.; Wang, S. Two-dimensional nanosheets associated with one-dimensional single-crystalline nanorods self-assembled into three-dimensional flower-like Mn_3O_4 hierarchical architectures. *Phys. Chem. Chem. Phys.* **2014**, *16*, 21742–21746. [CrossRef]
53. Nagamuthu, S.; Vijayakumar, S.; Muralidharan, G. Synthesis of Mn_3O_4/Amorphous Carbon Nanoparticles as Electrode Material for High Performance Supercapacitor Applications. *Energy Fuels* **2013**, *27*, 3508–3515. [CrossRef]
54. Gupta, A.; Chen, G.; Joshi, P.; Tadigadapa, S.; Eklund, P.C. Raman Scattering from High-Frequency Phonons in Supported n-Graphene Layer Films. *Nano Lett.* **2006**, *6*, 2667–2673. [CrossRef] [PubMed]
55. Lou, X.; Wu, X.; Zhang, Y. A study about γ-MnOOH nanowires as anode materials for rechargeable Li-ion batteries. *J. Alloys Compd.* **2013**, *550*, 185–189. [CrossRef]
56. Yan, Y.; Zhu, Y.; Yu, Y.; Li, J.; Mei, T.; Ju, Z.; Qian, Y. MnCO3 Microstructures Assembled with Nanoparticles: Shape-Controlled Synthesis and Their Application for Li-Ion Batteries. *J. Nanosci. Nanotechnol.* **2012**, *12*, 7334–7338. [CrossRef]
57. Gao, M.; Cui, X.; Wang, R.; Wang, T.; Chen, W. Graphene-wrapped mesoporous MnCO3 single crystals synthesized by a dynamic floating electrodeposition method for high performance lithium-ion storage. *J. Mater. Chem. A* **2015**, *3*, 14126–14133. [CrossRef]
58. Poizot, P.; Laruelle, S.; Grugeon, S.; Dupont, L.; Tarascon, J.M. Nano-sized transition-metal oxides as negative-electrode materials for lithium-ion batteries. *Nature* **2000**, *407*, 496–499. [CrossRef]
59. Palaniyandy, N.; Nkosi, F.P.; Raju, K.; Ozoemena, K.I. Conversion of electrolytic MnO_2 to Mn_3O_4 nanowires for high-performance anode materials for lithium-ion batteries. *J. Electroanal. Chem.* **2019**, *833*, 79–92. [CrossRef]
60. Wang, B.; Li, F.; Wang, X.; Wang, G.; Wang, H.; Bai, J. Mn_3O_4 nanotubes encapsulated by porous graphene sheets with enhanced electrochemical properties for lithium/sodium-ion batteries. *Chem. Eng. J.* **2019**, *364*, 57–69. [CrossRef]
61. Xu, L.; Chen, X.; Zeng, L.; Liu, R.; Zheng, C.; Qian, Q.; Chen, Q. Synthesis of hierarchical Mn_3O_4 microsphere composed of ultrathin nanosheets and its excellent long-term cycling performance for lithium-ion batteries. *J. Mater. Sci. Mater. El.* **2019**, *30*, 3055–3060. [CrossRef]
62. Jiang, Z.; Huang, K.; Yang, D.; Wang, S.; Zhong, H.; Jiang, C. Facile preparation of Mn_3O_4 hollow microspheres via reduction of pentachloropyridine and their performance in lithium-ion batteries. *RSC Adv.* **2017**, *7*, 8264–8271. [CrossRef]
63. Huang, S.-Z.; Jin, J.; Cai, Y.; Li, Y.; Tan, H.-Y.; Wang, H.-E.; Van Tendeloo, G.; Su, B.-L. Engineering single crystalline Mn_3O_4 nano-octahedra with exposed highly active {011} facets for high performance lithium ion batteries. *Nanoscale* **2014**, *6*, 6819–6827. [CrossRef] [PubMed]
64. Zhen, M.; Zhang, Z.; Ren, Q.; Liu, L. Room-temperature synthesis of ultrathin Mn_3O_4 nanosheets as anode materials for lithium-ion batteries. *Mater. Lett.* **2016**, *177*, 21–24. [CrossRef]
65. Yang, Y.; Huang, X.; Xiang, Y.; Chen, S.; Guo, L.; Leng, S.; Shi, W. Mn_3O_4 with different morphologies tuned through one-step electrochemical method for high-performance lithium-ion batteries anode. *J. Alloys Compd.* **2019**, *771*, 335–342. [CrossRef]
66. Ivanishchev, A.V.; Ivanishcheva, I.A.; Dixit, A. LiFePO4-Based Composite Electrode Material: Synthetic Approaches, Peculiarities of the Structure, and Regularities of Ionic Transport Processes. *Russ. J. Electrochem.* **2019**, *55*, 719–737. [CrossRef]
67. Ivanishchev, A.V.; Churikov, A.V.; Ivanishcheva, I.A.; Ushakov, A.V. Lithium diffusion in Li3V2(PO4)3-based electrodes: A joint analysis of electrochemical impedance, cyclic voltammetry, pulse chronoamperometry, and chronopotentiometry data. *Ionics* **2016**, *22*, 483–501. [CrossRef]

68. Ivanishchev, A.V.; Churikov, A.V.; Ushakov, A.V. Lithium transport processes in electrodes on the basis of Li3V2(PO4)3 by constant current chronopotentiometry, cyclic voltammetry and pulse chronoamperometry. *Electrochim. Acta* **2014**, *122*, 187–196. [CrossRef]
69. Bai, Z.; Zhang, X.; Zhang, Y.; Guo, C.; Tang, B. Facile synthesis of mesoporous Mn_3O_4 nanorods as a promising anode material for high performance lithium-ion batteries. *J. Mater. Chem. A* **2014**, *2*, 16755–16760. [CrossRef]
70. Wang, J.; Du, N.; Wu, H.; Zhang, H.; Yu, J.; Yang, D. Order-aligned Mn_3O_4 nanostructures as super high-rate electrodes for rechargeable lithium-ion batteries. *J. Power Sources* **2013**, *222*, 32–37. [CrossRef]
71. Bai, Z.; Fan, N.; Ju, Z.; Guo, C.; Qian, Y.; Tang, B.; Xiong, S. Facile synthesis of mesoporous Mn_3O_4 nanotubes and their excellent performance for lithium-ion batteries. *J. Mater. Chem. A* **2013**, *1*, 10985–10990. [CrossRef]
72. Guo, J.; Liu, Q.; Wang, C.; Zachariah, M.R. Interdispersed Amorphous MnOx–Carbon Nanocomposites with Superior Electrochemical Performance as Lithium-Storage Material. *Adv. Funct. Mater.* **2012**, *22*, 803–811. [CrossRef]
73. Wu, Y.; Yue, K.; Wang, Y.; Chen, C.; Lü, W.; Duan, L. Controlled synthesis of MnOOH multilayer nanowires as anode materials for lithium-ion batteries. *Mater. Charact.* **2016**, *118*, 405–410. [CrossRef]
74. Cao, Y.; Xiao, L.; Ai, X.; Yang, H. Surface-Modified Graphite as an Improved Intercalating Anode for Lithium-Ion Batteries. *Electrochem. Solid-State Lett.* **2003**, *6*, A30–A33. [CrossRef]
75. Hao, Q.; Wang, J.; Xu, C. Facile preparation of Mn_3O_4 octahedra and their long-term cycle life as an anode material for Li-ion batteries. *J. Mater. Chem. A* **2014**, *2*, 87–93. [CrossRef]
76. Yonekura, D.; Iwama, E.; Ota, N.; Muramatsu, M.; Saito, M.; Orikasa, Y.; Naoi, W.; Naoi, K. Progress of the conversion reaction of Mn_3O_4 particles as a function of the depth of discharge. *Phys. Chem. Chem. Phys.* **2014**, *16*, 6027–6032. [CrossRef]
77. Alfaruqi, M.H.; Gim, J.; Kim, S.; Song, J.; Duong, P.T.; Jo, J.; Baboo, J.P.; Xiu, Z.; Mathew, V.; Kim, J. One-Step Pyro-Synthesis of a Nanostructured Mn_3O_4/C Electrode with Long Cycle Stability for Rechargeable Lithium-Ion Batteries. *Chem. Eur. J.* **2016**, *22*, 2039–2045. [CrossRef]
78. Ivanishchev, A.V.; Bobrikov, I.A.; Ivanishcheva, I.A.; Ivanshina, O.Y. Study of structural and electrochemical characteristics of LiNi0.33Mn0.33Co0.33O2 electrode at lithium content variation. *J. Electroanal. Chem.* **2018**, *821*, 140–151. [CrossRef]
79. Ivanishchev, A.V.; Churikov, A.V.; Ivanishcheva, I.A.; Ushakov, A.V.; Sneha, M.J.; Babbar, P.; Dixit, A. Models of lithium transport as applied to determination of diffusion characteristics of intercalation electrodes. *Russ. J. Electrochem.* **2017**, *53*, 706–712. [CrossRef]
80. Ivanishcheva, I.A.; Ivanishchev, A.V.; Dixit, A. Positive effect of surface modification with titanium carbosilicide on performance of lithium-transition metal phosphate cathode materials. *Monatsh. Chem.* **2019**, *150*, 489–498. [CrossRef]
81. Zhang, R.; Jing, X.; Chu, Y.; Wang, L.; Kang, W.; Wei, D.; Li, H.; Xiong, S. Nitrogen/oxygen co-doped monolithic carbon electrodes derived from melamine foam for high-performance supercapacitors. *J. Mater. Chem. A* **2018**, *6*, 17730–17739. [CrossRef]